LETTERS

A strong ferroelectric ferromagnet created by means of spin–lattice coupling

June Hyuk Lee[1,2], Lei Fang[3]*, Eftihia Vlahos[2]*, Xianglin Ke[4]*, Young Woo Jung[3], Lena Fitting Kourkoutis[5], Jong-Woo Kim[6], Philip J. Ryan[6], Tassilo Heeg[1], Martin Roeckerath[7], Veronica Goian[8], Margitta Bernhagen[9], Reinhard Uecker[9], P. Chris Hammel[3], Karin M. Rabe[10], Stanislav Kamba[8], Jürgen Schubert[7], John W. Freeland[6], David A. Muller[5,11], Craig J. Fennie[5], Peter Schiffer[4], Venkatraman Gopalan[2], Ezekiel Johnston-Halperin[3] & Darrell G. Schlom[1]

Ferroelectric ferromagnets are exceedingly rare, fundamentally interesting multiferroic materials that could give rise to new technologies in which the low power and high speed of field-effect electronics are combined with the permanence and routability of voltage-controlled ferromagnetism[1,2]. Furthermore, the properties of the few compounds that simultaneously exhibit these phenomena[1–5] are insignificant in comparison with those of useful ferroelectrics or ferromagnets: their spontaneous polarizations or magnetizations are smaller by a factor of 1,000 or more. The same holds for magnetic- or electric-field-induced multiferroics[6–8]. Owing to the weak properties of single-phase multiferroics, composite and multilayer approaches involving strain-coupled piezoelectric and magnetostrictive components are the closest to application today[1,2]. Recently, however, a new route to ferroelectric ferromagnets was proposed[9] by which magnetically ordered insulators that are neither ferroelectric nor ferromagnetic are transformed into ferroelectric ferromagnets using a single control parameter, strain. The system targeted, EuTiO$_3$, was predicted to exhibit strong ferromagnetism (spontaneous magnetization, ~7 Bohr magnetons per Eu) and strong ferroelectricity (spontaneous polarization, ~10 μC cm^{-2}) simultaneously under large biaxial compressive strain[9]. These values are orders of magnitude higher than those of any known ferroelectric ferromagnet and rival the best materials that are solely ferroelectric or ferromagnet. Hindered by the absence of an appropriate substrate to provide the desired compression we turned to tensile strain. Here we show both experimentally and theoretically the emergence of a multiferroic state under biaxial tension with the unexpected benefit that even lower strains are required, thereby allowing thicker high-quality crystalline films. This realization of a strong ferromagnetic ferroelectric points the way to high-temperature manifestations of this spin–lattice coupling mechanism[10]. Our work demonstrates that a single experimental parameter, strain, simultaneously controls multiple order parameters and is a viable alternative tuning parameter to composition[11] for creating multiferroics.

Using epitaxy and the mis-fit strain imposed by an underlying substrate, it is possible to strain dielectric thin films to per cent levels—far beyond where they would crack in bulk. Such strains are used to enhance the mobility of transistors[12] and increase superconducting[13], ferromagnetic[14,15] and ferroelectric[16] transition temperatures. In fact, it

has been shown experimentally and theoretically that such strains can even stabilize systems in novel non-bulk phases, for example SrTiO$_3$ in ferroelectric phases[17,18].

Recently a route to achieving simultaneously strong ferromagnetism and ferroelectricity in a single phase has been proposed[9]. This technique makes use of a generic mechanism in which the electron spin couples to the lattice:

$$\omega^2 = \omega_0^2 - \lambda \left\langle \mathbf{S}_i \bullet \mathbf{S}_j \right\rangle \qquad (1)$$

Here ω is the frequency of an infrared-active phonon (lattice) mode, ω_0 is the bare phonon frequency, λ is the macroscopic spin–phonon coupling constant and $\langle \mathbf{S}_i \bullet \mathbf{S}_j \rangle$ is the nearest-neighbour spin–spin correlation function. Such spin–lattice coupling normally leads to magnetocapacitance[19], but in theory[9] this term, in conjunction with strain, could tune multiple ferroic order parameters simultaneously, resulting in the emergence of new ground states[9]. A simple model that captures the essential physics of this tuning behaviour can be written as a first-order transition induced by a biquadratic coupling of lattice and magnetic order parameters:

$$\mathcal{F}(\mathbf{M},\mathbf{P}) = \frac{A_P \mathbf{P}^2}{2} + \frac{A_M \mathbf{M}^2}{2} + \frac{B_P \mathbf{P}^4}{4} + \frac{B_M \mathbf{M}^4}{4} - |\lambda'||\mathbf{M}^2 \mathbf{P}^2$$

$$\mathcal{F}(\mathbf{L},\mathbf{P}) = \frac{A_P \mathbf{P}^2}{2} + \frac{A_L \mathbf{L}^2}{2} + \frac{B_P \mathbf{P}^4}{4} + \frac{B_L \mathbf{L}^4}{4} + |\lambda'||\mathbf{L}^2 \mathbf{P}^2$$

Here $\mathcal{F}$ is the Landau free energy, $\mathbf{P}$, $\mathbf{M}$ and $\mathbf{L}$ are the ferroelectric, ferromagnetic and antiferromagnetic order parameters, respectively, and A_P, B_P, A_M, B_M, A_L and B_L are expansion coefficients. The sign and strength of the biquadratic coupling coefficient, λ', which is positive for antiferromagnetic order and negative for ferromagnetic order, originates in the spin–lattice coupling and is fundamental to the tuning behaviour. Such biquadratic magnetoelectric coupling, as well its change of sign under magnetic bias, was recently confirmed for unstrained bulk EuTiO$_3$ and was found to be large[20]. The above model led to the prediction[9] that (001) EuTiO$_3$ would transform from its paraelectric and antiferromagnetic unstrained ground state[19] to a simultaneously ferromagnetic and ferroelectric ground state for compressive strains exceeding 1.2%.

Owing to the lack of appropriate substrates and the high strains involved for those that do exist (for example, a commensurate EuTiO$_3$

[1]Department of Materials Science and Engineering, Cornell University, Ithaca, New York 14853-1501, USA. [2]Department of Materials Science and Engineering, Pennsylvania State University, University Park, Pennsylvania 16802-5005, USA. [3]Department of Physics, Ohio State University, Columbus, Ohio 43210-1117, USA. [4]Department of Physics and Materials Research Institute, Pennsylvania State University, University Park, Pennsylvania 16802, USA. [5]School of Applied and Engineering Physics, Cornell University, Ithaca, New York 14853, USA. [6]Advanced Photon Source, Argonne National Laboratory, Argonne, Illinois 60439, USA. [7]Institute of Bio and Nanosystems, JARA-Fundamentals of Future Information Technologies, Research Centre Jülich, D-52425 Jülich, Germany. [8]Institute of Physics ASCR, Na Slovance 2, 182 21 Prague 8, Czech Republic. [9]Leibniz Institute for Crystal Growth, Max-Born-Straße 2, D-12489 Berlin, Germany. [10]Department of Physics and Astronomy, Rutgers University, Piscataway, New Jersey 08854-8019, USA. [11]Kavli Institute at Cornell for Nanoscale Science, Ithaca, New York 14853, USA.
*These authors contributed equally to this work.
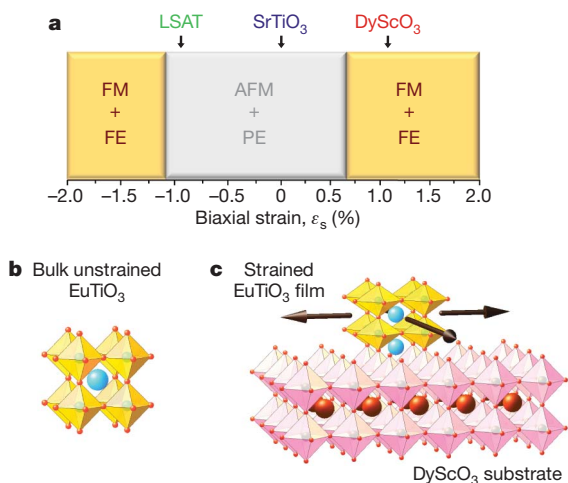
Figure 1 | Predicted effect of biaxial strain on EuTiO₃ and our approach to imparting such strain in EuTiO₃ films using epitaxy. **a**, First-principles epitaxial phase diagram of $EuTiO_3$ strained from −2% (biaxial compression) to +2% (biaxial tension), calculated in 0.1% steps. Regions with paraelectric (PE), ferroelectric (FE), antiferromagnetic (AFM) and ferromagnetic (FM) behaviour are shown. **b, c**, Schematic of unstrained bulk $EuTiO_3$ (**b**) and epitaxially strained thin-film $EuTiO_3$ on the $DyScO_3$ substrate (**c**), showing the in-plane expansion due to biaxial tension.

film on a $LaAlO_3$ substrate would have a biaxial strain of $\varepsilon_s \approx -2.9\%$), we are not able to experimentally achieve the biaxial compression required while maintaining a high-quality crystalline film. This leads us to extend the calculated strain phase diagram of (001) $EuTiO_3$, which previously considered only the effect of biaxial compression[9], to include biaxial tension (Fig. 1a). By doing so (Supplementary

Discussion 1), we find that the theoretical critical strain to reach the ferroelectric ferromagnetic ground state is lower in biaxial tension ($\varepsilon_s = +0.75\%$) than in biaxial compression ($\varepsilon_s = -1.2\%$). Lower strains are experimentally appealing as they allow thicker commensurately strained films to be grown, provided that suitable substrates exist. Tensile strain has the added advantage that the ferroelectric polarization is in-plane, eliminating the importance of finite-size effects associated with depolarization fields[21,22]. To assess the theoretical phase diagram, we prepare commensurate $EuTiO_3$ films on substrates in the same structural family (perovskites) with lattice constants suitably close to that of $EuTiO_3$ so films thick enough to test for ferroelectricity and ferromagnetism can be grown. Commensurate films reduce the complicating influence of dislocations on film properties[23]. Our approach is illustrated in Fig. 1b, c.

Our experiments are performed on 22-nm-thick commensurate (001)-oriented $EuTiO_3$ films grown by reactive molecular-beam epitaxy[24] on (001) $(LaAlO_3)_{0.29}$–$(SrAl_{1/2}Ta_{1/2}O_3)_{0.71}$ (LSAT), (001) $SrTiO_3$ and (110) $DyScO_3$ substrates. These substrates impart biaxial strains of −0.9%, 0.0% and about +1.1%, respectively. The structural, ferroelectric and ferromagnetic properties of these films (in addition to multiple control samples including bare substrates) are measured to assess the predictions of Fig. 1a.

X-ray diffraction (Fig. 2a) and cross-sectional scanning transmission electron microscopy (STEM; Fig. 2b) reveal the films to be commensurate, smooth and of high structural perfection. Cross-sectional chemical mapping of the interface between the $EuTiO_3$ film and the $DyScO_3$ substrate at atomic resolution (Fig. 2b) demonstrates that the interface between the film and the substrate is abrupt.

Temperature-dependent second harmonic generation (SHG) measurements (Fig. 3a) indicate the paraelectric-to-ferroelectric transition temperature (T_c) of the films. Materials lacking inversion symmetry exhibit SHG and ferroelectrics lack inversion symmetry.
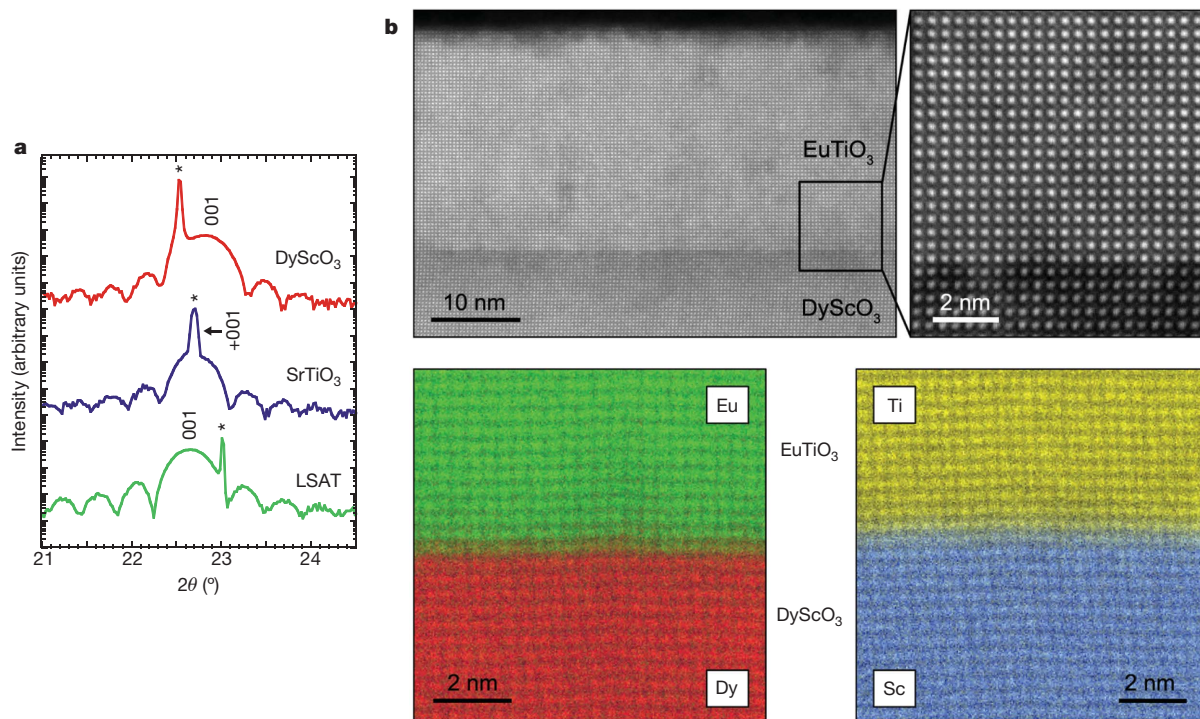
Figure 2 | Structural characterization by X-ray diffraction and STEM of 22-nm-thick commensurate epitaxial EuTiO₃ films. **a**, θ–2θ X-ray diffraction scans of $EuTiO_3$ on $DyScO_3$ (red), $EuTiO_3$ on $SrTiO_3$ (blue) and $EuTiO_3$ on LSAT (green) in the vicinity of the out-of-plane 001_p $EuTiO_3$ reflection, where the subscript refers to pseudocubic indices. Clear thickness fringes are seen. The substrate peaks are denoted with asterisks. **b**, Annular dark-field and spectroscopic imaging of the $EuTiO_3$-on-$DyScO_3$ heterostructure characterized in **a**. Top: annular dark-field/STEM images of the structure showing a coherent interface and a low density of defects in the $EuTiO_3$ film. Bottom: A-site and B-site elemental maps of the interface obtained by combining the Eu-$M_{4,5}$ (green) and Dy-$M_{4,5}$ (red) electron energy-loss spectroscopy edges, and the Ti-$L_{2,3}$ (yellow) and Sc-$L_{2,3}$ (blue) edges extracted from two separate 256×256-pixel spectrum image acquisitions (one for the Eu/Dy edges, the other for the Sc/Ti edges). Intermixing is limited to one to two atomic layers at the interface.
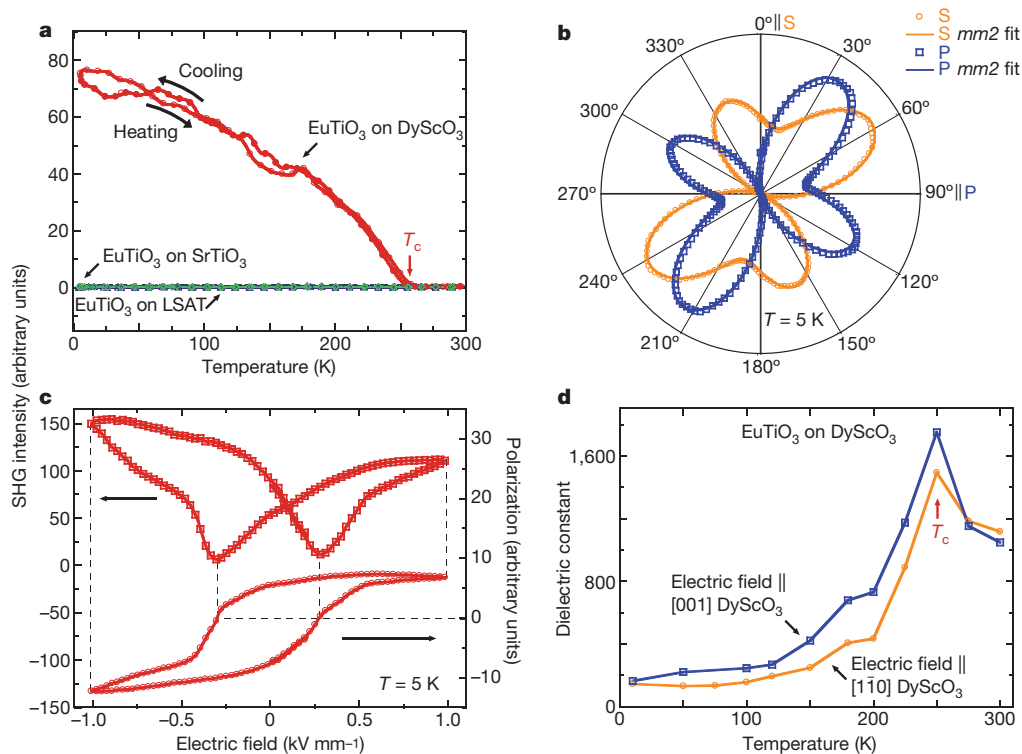
Figure 3 | Commensurate EuTiO₃ strained in biaxial tension at +1.1% on DyScO₃ is ferroelectric below $T_c \approx 250$ K. a, Temperature dependence of the SHG signal of EuTiO₃ on DyScO₃ (red), EuTiO₃ on SrTiO₃ (blue) and EuTiO₃ on LSAT (green). **b,** Experimental polar plots (points) and *mm*2 fit (line) with analyser along ⟨100⟩ₚ directions for EuTiO₃ on DyScO₃ at 5 K. The P and S polarizations are in and perpendicular to the incidence plane, respectively, where the incidence plane is formed by the sample normal and the direction of propagation of the incident light field. **c,** SHG hysteresis loop (top) and corresponding polarization loop (bottom) for EuTiO₃ on DyScO₃ at 5 K. **d,** Dielectric constant versus temperature for a nearly commensurate ($\varepsilon_s = +1.1\%$) 100-nm-thick EuTiO₃-on-DyScO₃ film, determined by far-infrared reflectance spectroscopy.

Therefore, SHG activity is a necessary but insufficient condition for ferroelectricity. Only the EuTiO₃-on-DyScO₃ film exhibits an SHG response, with $T_c \approx 250$ K. The absence of an SHG response from the EuTiO₃ strained at $\varepsilon_s = -0.9\%$ (EuTiO₃ on LSAT) and $\varepsilon_s = 0.0\%$ (EuTiO₃ on SrTiO₃) indicates that EuTiO₃ in these strain states is not ferroelectric.

Having determined that the EuTiO₃ film strained at $\varepsilon_s = +1.1\%$ (EuTiO₃ on DyScO₃) is potentially ferroelectric, we ask whether it satisfies additional ferroelectric criteria: a polar point group; a peak in dielectric constant versus temperature at T_c; and changes in domain populations when an electric field is applied. To establish the point group symmetry, we make SHG polar plots (Fig. 3b). The experimental data fit well with the *mm*2 polar point group model. This result is consistent with the first-principles calculations. We probe domain dynamics by monitoring the SHG intensity as a function of applied in-plane electric field (Fig. 3c).

We make an additional test of the ferroelectric phase transition by measuring the dielectric constant as a function of temperature in a strained EuTiO₃-on-DyScO₃ film. Owing to the low bandgap of EuTiO₃ (0.9 eV; ref. 24) and associated leakage issues, the low-frequency dielectric constant is extracted from far-infrared reflectance measurements on a 100-nm-thick EuTiO₃-on-DyScO₃ film (Fig. 3d and Supplementary Discussion 2). A peak in dielectric constant as a function of temperature is clearly seen at a temperature comparable to that at which the onset of the phase transition revealed by SHG occurs (Fig. 3a). The dielectric anomaly is caused by an optical soft mode, which has a frequency minimum at T_c (Supplementary Fig. 1). This anomaly is additional evidence for the ferroelectric phase transition in strained EuTiO₃ on DyScO₃. All these results are consistent with EuTiO₃ strained at $\varepsilon_s = +1.1\%$ undergoing a paraelectric-to-ferroelectric transition at about 250 K.

Testing for ferromagnetism in strained EuTiO₃-on-DyScO₃ films is complicated by the large paramagnetic response of the DyScO₃ substrate. If a superconducting quantum interference device (SQUID) magnetometer is used under typical measurement magnetic fields, the paramagnetic response of the thick substrate swamps the signal from the strained EuTiO₃ film. For this reason, we use a combination of the magneto-optic Kerr effect (MOKE) and SQUID magnetometry. Exploiting the optical nature of the MOKE technique, the probe is tuned to a wavelength between 690 nm and 750 nm to maximize the absorption in the EuTiO₃ epilayer while minimizing interactions with the substrate. This renders the measurement insensitive to the paramagnetic substrates as well as to the antiferromagnetic state of DyScO₃ below its Néel temperature, $T_N = 3.1$ K (ref. 25). The MOKE response from all three EuTiO₃ films and a bare DyScO₃ substrate is shown in Fig. 4a. The EuTiO₃ strained at $\varepsilon_s = +1.1\%$ (EuTiO₃ on DyScO₃) has a clear ferromagnetic hysteresis loop, with sharp switching to full saturation, signifying that it is ferromagnetic, in contrast to the EuTiO₃ with $\varepsilon_s = -0.9\%$ (EuTiO₃ on LSAT) or $\varepsilon_s = 0.0\%$ (EuTiO₃ on SrTiO₃). The temperature dependence of the MOKE (Fig. 4b) shows that the Curie temperature of the sample strained at $\varepsilon_s = +1.1\%$ is $T_C = 4.24 \pm 0.02$ K (Supplementary Discussion 3), which is slightly lower than 5.5 K, the Néel temperature of unstrained EuTiO₃ (refs 19, 24).

Because the MOKE measurements of ferromagnetism are not on an absolute scale, we use SQUID measurements to quantify the spontaneous magnetization of EuTiO₃ strained at $\varepsilon_s = +1.1\%$. These measurements are made in nominally zero residual magnetic field to minimize the paramagnetic response of the substrate. The strained EuTiO₃ is cooled in a 100-Oe field, which is high enough to polarize the EuTiO₃ film yet small enough to minimize the residual magnetic field during subsequent SQUID measurements. The observed magnetization (Fig. 4b) is seen to rise at the same temperature (T_C) as the MOKE signal and follows it until the antiferromagnetic transition of the DyScO₃ substrate occurs, at 3.1 K, where the substrate signal masks the magnetization of the strained EuTiO₃ film. In agreement with the
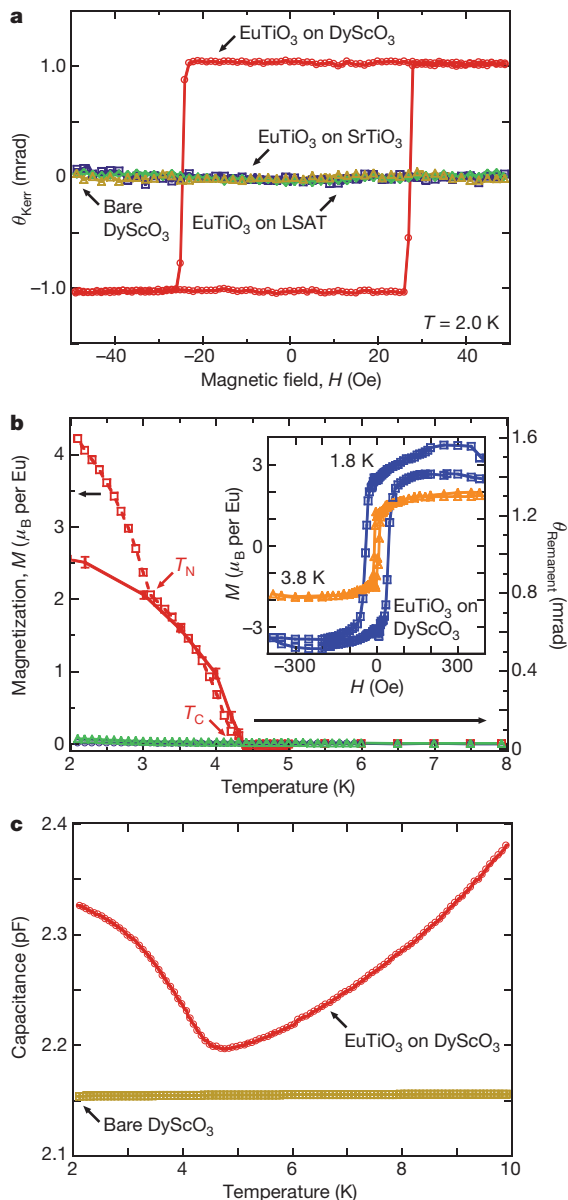
Figure 4 | Magnetization and capacitance measurements showing that EuTiO$_3$ on DyScO$_3$ is ferromagnetic below T_C = 4.24 ± 0.02 K and that these two quantities are coupled. a, MOKE measurements at 2.0 K of EuTiO$_3$ on DyScO$_3$ (red), EuTiO$_3$ on SrTiO$_3$ (blue), EuTiO$_3$ on LSAT (green) and bare DyScO$_3$ substrate (gold). θ_{Kerr} is the Kerr-induced polarization rotation in the optical probe beam and is proportional to the in-plane magnetization. **b,** Temperature dependence of the magnetization measured using both the MOKE and a SQUID. Inset, isothermal SQUID magnetization curves at T = 1.8 and 3.8 K. The red data points with error bars (representing 1σ variations for both temperature and θ_{Kerr}) show the temperature dependence of the remanent value of θ_{Kerr} for EuTiO$_3$ on DyScO$_3$, $\theta_{Remanent}$. μ_B, Bohr magneton. **c,** Temperature dependence of the capacitance of EuTiO$_3$ on DyScO$_3$ near T_C. The capacitance of a bare DyScO$_3$ substrate measured under the same conditions is also shown.

MOKE results, clear hysteresis loops are observed below 4 K (Fig. 4b, inset) and the spontaneous magnetization of the strained EuTiO$_3$ is seen to be large, that is, several Bohr magnetons per Eu. Polarized X-ray measurements of the local moment connect the observed magnetism with that of Eu^{2+} (Supplementary Discussion 4). From the combination of these results, and because the ferromagnetism occurs well above the antiferromagnetic transition of the DyScO$_3$ substrate, we conclude that the observed ferromagnetism is not correlated with the magnetic ordering of the underlying substrate.

Bulk EuTiO$_3$ exhibits a decrease in its dielectric constant as it is cooled through its antiferromagnetic transition[19]. Owing to the change in the sign of the spin–spin correlation function in equation (1) when strained EuTiO$_3$ becomes ferromagnetic, the dielectric constant of EuTiO$_3$ on DyScO$_3$ should increase as the film is cooled through its ferromagnetic transition. Such behaviour was observed (Fig. 4c), further corroborating the ferromagnetic transition in commensurately strained EuTiO$_3$ on DyScO$_3$ and its strong spin–lattice coupling.

Our results confirm the theorized mechanism[9] and open the door to higher-temperature implementations of strong ferromagnetic ferroelectrics[10], which would allow for dramatic improvements in numerous devices and applications: magnetic sensors[26], energy harvesting, high-density multistate memory elements[27], wireless powering of miniature systems[28], and tunable microwave filters, delay lines, phase shifters and resonators[29,30].

METHODS SUMMARY

We performed first-principles density functional calculations using projector-augmented-wave potentials within spin-polarized GGA + U approximation as implemented in the Vienna *Ab-initio* Simulation Package (Supplementary Discussion 1). We grew EuTiO$_3$ thin films by reactive molecular-beam epitaxy[24], from elemental europium and titanium sources at a substrate temperature of 650 °C in a background partial pressure of molecular oxygen of 3×10^{-8} torr. EuTiO$_3$ films in three strain states (EuTiO$_3$ on DyScO$_3$, EuTiO$_3$ on SrTiO$_3$ and EuTiO$_3$ on LSAT; see Supplementary Table 1), as well as bare substrates, were characterized structurally by X-ray diffraction (Supplementary Discussions 5 and 6) and STEM; chemically by STEM/electron energy-loss spectroscopy, Rutherford backscattering spectrometry (Supplementary Fig. 2) and X-ray absorption spectroscopy (Supplementary Discussion 4); (iii) for ferroelectricity by SHG (Supplementary Discussion 7) and far-infrared reflectance (Supplementary Discussion 2); (iv) for ferromagnetism using the MOKE (Supplementary Discussion 3) and a SQUID (Supplementary Fig. 3); and (v) for the temperature dependence of capacitance (Supplementary Discussion 8).

Full Methods and any associated references are available in the online version of the paper at www.nature.com/nature.

1. Eerenstein, W., Mathur, N. D. & Scott, J. F. Multiferroic and magnetoelectric materials. *Nature* **442**, 759–765 (2006).
2. Ramesh, R. & Spaldin, N. A. Multiferroics: progress and prospects in thin films. *Nature Mater.* **6**, 21–29 (2007).
3. Rivera, J.-P. & Schmid, H. Electrical and optical measurements on nickel iodine boracite. *Ferroelectrics* **36**, 447–450 (1981).
4. Ikeda, N. *et al.* Ferroelectricity from iron valence ordering in the charge-frustrated system LuFe$_2$O$_4$. *Nature* **436**, 1136–1138 (2005).
5. Park, J. Y., Park, J. H., Jeong, Y. K. & Jang, H. M. Dynamic magnetoelectric coupling in "electronic ferroelectric" LuFe$_2$O$_4$. *Appl. Phys. Lett.* **91**, 152903 (2007).
6. Kimura, T. *et al.* Magnetic control of ferroelectric polarization. *Nature* **426**, 55–58 (2003).
7. Lottermoser, T. *et al.* Magnetic phase control by an electric field. *Nature* **430**, 541–544 (2004).
8. Kimura, T., Sekio, Y., Nakamura, H., Siegrist, T. & Ramirez, A. P. Cupric oxide as an induced-multiferroic with high-T_C. *Nature Mater.* **7**, 291–294 (2008).
9. Fennie, C. J. & Rabe, K. M. Magnetic and electric phase control in epitaxial EuTiO$_3$ from first principles. *Phys. Rev. Lett.* **97**, 267602 (2006).
10. Lee, J. H. & Rabe, K. M. Epitaxial-strain-induced multiferroicity in SrMnO$_3$ from first principles. *Phys. Rev. Lett.* **104**, 207204 (2010).
11. Goto, T., Kimura, T., Lawes, G., Ramirez, A. P. & Tokura, Y. Ferroelectricity and giant magnetocapacitance in perovskite rare-earth manganites. *Phys. Rev. Lett.* **92**, 257201 (2004).
12. Nguyen, L. D., Brown, A. S., Thompson, M. A. & Jelloian, L. M. 50-nm self-aligned-gate pseudomorphic AlInAs/GaInAs high electron mobility transistors. *IEEE Trans. Electron. Dev.* **39**, 2007–2014 (1992).
13. Bozovic, I., Logvenov, G., Belca, I., Narimbetov, B. & Sveklo, I. Epitaxial strain and superconductivity in La$_{2-x}$Sr$_x$CuO$_4$ thin films. *Phys. Rev. Lett.* **89**, 107001 (2002).
14. Beach, R. S. *et al.* Enhanced Curie temperatures and magnetoelastic domains in Dy/Lu superlattices and films. *Phys. Rev. Lett.* **70**, 3502–3505 (1993).
15. Fuchs, D. *et al.* Tuning the magnetic properties of LaCoO$_3$ thin films by epitaxial strain. *Phys. Rev. B* **77**, 014434 (2008).
16. Choi, K. J. *et al.* Enhancement of ferroelectricity in strained BaTiO$_3$ thin films. *Science* **306**, 1005–1009 (2004).
17. Pertsev, N. A., Tagantsev, A. K. & Setter, N. Phase transitions and strain-induced ferroelectricity in SrTiO$_3$ epitaxial thin films. *Phys. Rev. B* **61**, R825–R829 (2000).
18. Haeni, J. H. *et al.* Room-temperature ferroelectricity in strained SrTiO$_3$. *Nature* **430**, 758–761 (2004).

19. Katsufuji, T. & Takagi, H. Coupling between magnetism and dielectric properties in quantum paraelectric $EuTiO_3$. *Phys. Rev. B* **64**, 054415 (2001).
20. Shvartsman, V. V., Borisov, P., Kleemann, W., Kamba, S., &. Katsufuji, T. Large off-diagonal magnetoelectric coupling in the quantum paraelectric antiferromagnet $EuTiO_3$. *Phys. Rev. B* **81**, 064426 (2010).
21. Junquera, J. & Ghosez, P. Critical thickness for ferroelectricity in perovskite ultrathin films. *Nature* **422**, 506–509 (2003).
22. Fong, D. D. *et al.* Ferroelectricity in ultrathin perovskite films. *Science* **304**, 1650–1653 (2004).
23. Chu, M.-W. *et al.* Impact of misfit dislocations on the polarization instability of epitaxial nanostructured ferroelectric perovskites. *Nature Mater.* **3**, 87–90 (2004).
24. Lee, J. H. *et al.* Optical band gap and magnetic properties of unstrained $EuTiO_3$ films. *Appl. Phys. Lett.* **94**, 212509 (2009).
25. Ke, X. *et al.* Low temperature magnetism in the perovskite substrate $DyScO_3$. *Appl. Phys. Lett.* **94**, 152503 (2009).
26. Zhai, J. Y., Xing, Z. P., Dong, S. X., Li, J. F. & Viehland, D. Detection of pico-Tesla magnetic fields using magneto-electric sensors at room temperature. *Appl. Phys. Lett.* **88**, 062510 (2006).
27. Gajek, M. *et al.* Tunnel junctions with multiferroic barriers. *Nature Mater.* **6**, 296–302 (2007).
28. Bayrashev, A., Robbins, W. P. & Ziaie, B. Low frequency wireless powering of microsystems using piezoelectric-magnetostrictive laminate composites. *Sens. Actuators A* **114**, 244–249 (2004).
29. Fetisov, Y. K. & Srinivasan, G. Electric field tuning characteristics of a ferrite-piezoelectric microwave resonator. *Appl. Phys. Lett.* **88**, 143503 (2006).
30. Das, J., Song, Y.-Y., Mo, N., Krivosik, P. & Patton, C. E. Electric-field-tunable low loss multiferroic ferrimagnetic-ferroelectric heterostructures. *Adv. Mater.* **21**, 2045–2049 (2009).

Author Contributions The first-principles calculations were performed by C.J.F. and K.M.R. The thin films were synthesized by J.H.L. and D.G.S. on single-crystal substrates including $DyScO_3$ grown by M.B. and R.U. The films were characterized using the MOKE by L.F., Y.W.J., P.C.H. and E.J.-H.; by SHG by E.V. and V. Gopalan; using a SQUID and by capacitance by X.K. and P.S.; by electron microscopy and spectroscopy by L.F.K. and D.A.M.; by X-ray diffraction by J.H.L., J.W.K. and P.J.R.; by X-ray absorption spectroscopy and X-ray magnetic circular dichroism by J.W.F.; by Rutherford backscattering spectrometry by T.H., M.R. and J.S.; and by far-infrared reflectance by V. Goian and S.K. D.G.S., C.J.F., J.W.F. and J.H.L. wrote the manuscript.

METHODS

EuTiO$_3$ is a cubic perovskite oxide (space group, $Pm\bar{3}m$) with a lattice constant $a = 3.905\,\text{Å}$ at room temperature[19,31]. This oxide is the subject of this study because its PE–AFM ground state lies very close to a phase transition shown in Fig. 1a. Owing to this sensitivity, it is imperative to select a thin-film growth technique that can yield the intrinsic properties of EuTiO$_3$. Reactive molecular-beam epitaxy[24] (MBE), in contrast to other methods used for EuTiO$_3$ film growth[32–36], is so far the only technique that has been able to achieve the intrinsic properties of unstrained EuTiO$_3$ as-grown films.

We grew EuTiO$_3$ thin films by MBE in an EPI 930 MBE chamber. Molecular beams of europium and titanium were generated using a conventional effusion cell and a Ti-Ball titanium sublimation pump[37], respectively. Each metal flux ($\sim 1.5 \times 10^{13}$ atoms cm^{-2} s^{-1}) was measured before growth using a quartz crystal microbalance calibrated by Rutherford backscattering spectrometry measurements. Europium and titanium were co-deposited onto the substrate under an oxygen background partial pressure of 3×10^{-8} torr. This oxygen partial pressure was found to be optimal for the growth of single-phase EuTiO$_3$ films with the desired oxidation states of Eu^{2+} and Ti^{4+}. The substrate temperature was 650 °C and the growth rate was $\sim 0.1\,\text{Å s}^{-1}$. *In situ* reflection high-energy electron diffraction images are consistent with the growth of smooth and epitaxial thin-film surfaces during deposition (Supplementary Fig. 4). Following deposition, the EuTiO$_3$ thin films were cooled under the same oxygen partial pressure in which they were grown.

Substrates. (001) LSAT, (001) SrTiO$_3$ and (110) DyScO$_3$ substrates were selected to induce biaxial strains of -0.9%, 0.0% and about $+1.1\%$ in EuTiO$_3$ films, respectively. These substrates are isostructural with EuTiO$_3$ (all are perovskites), are commercially available with high structural perfection and have lattice constants in the region of interest to test the predictions of Fig. 1a (ref. 38). In addition, SrTiO$_3$ and LSAT are non-magnetic, which simplifies magnetic characterization. LSAT is technically tetragonal although its c/a structural distortion is small enough (0.9995) that we treat it is if it were cubic with $a = 3.869\,\text{Å}$ (ref. 39). SrTiO$_3$ is cubic at room temperature and has a lattice constant $a = 3.905\,\text{Å}$ (ref. 40), which is nearly the same as the corresponding lattice constant in EuTiO$_3$. The (001) SrTiO$_3$ substrate was treated in buffered HF for 30 s and annealed at 950 °C for 1 h to obtain TiO$_2$ termination on the surface before EuTiO$_3$ film growth[41]. DyScO$_3$ is orthorhombic with lattice constants $a = 5.440\,\text{Å}$, $b = 5.717\,\text{Å}$ and $c = 7.903\,\text{Å}$ (ref. 42). The (110) DyScO$_3$ surface has a rectangular surface mesh that strains EuTiO$_3$ by $+1.0\%$ along the $[1\bar{1}0]_{\text{DyScO}_3}$ in-plane direction and by $+1.2\%$ along the perpendicular $[001]_{\text{DyScO}_3}$ in-plane direction. The (110) DyScO$_3$ substrate was annealed at 1,000 °C for 13 h in flowing oxygen at 1-atm pressure to promote a ScO$_2$-terminated surface.

Theory. In density functional theory, the failure of the generalized gradient approximation (GGA) properly to capture the physics of strongly correlated systems is well established. A widely accepted approach beyond GGA is the GGA plus Hubbard U (GGA + U) method[43]. We performed first-principles density functional calculations using projector-augmented-wave (PAW) potentials within the spin-polarized GGA + U approximation as implemented in the Vienna *Ab-initio* Simulation Package[44–47] with a plane-wave cut-off of 500 eV and an $8 \times 8 \times 8$ Γ-centred k-point mesh. The PAW potential for Eu treated the $4f^7 5s^2 5p^6 6s^2$ states as valence states. All calculations were performed with collinear spins and without spin–orbit coupling. As expected for Eu^{2+}, which lacks orbital degrees of freedom, inclusion of spin–orbit coupling does not change the results. Values of the Eu on-site Coulomb parameter, $U = 5.7$ eV, and exchange parameter, $J_{\text{H}} = 1.0$ eV, were used that give a reasonable account of the magnetic exchange constants which were extracted by mapping GGA + U calculations of the total energy for different spin configurations at $T = 0$ onto a classical Heisenberg model, $E_{\text{spin}} = -\Sigma_{ij} J_{ij} \langle \mathbf{S}_i \bullet \mathbf{S}_j \rangle$ (in our notation, the energy per spin bond is $2J$). We note that, given the relatively small energies involved, electronic relaxations converged to less than 10^{-7} eV and ionic relaxations were performed until residual forces reached less than 0.5×10^{-3} eV Å^{-1}. Phonon frequencies were calculated using the direct method where each ion was moved by approximately 0.01 Å and also using density functional perturbation theory as implemented in the Vienna *Ab-initio* Simulation Package. Calculations with the GGA + U approximation overestimate the lattice constant by $\sim 1\%$. We introduce a shift of the zero of σ_{33}, the out-of-plane component of the stress, so that $\sigma_{33} = 0$ for the cubic structure at the experimental lattice constant, $a_{\text{exp}} = 3.9\,\text{Å}$. Thus, the correct cubic structure is obtained at mis-fit strain $\eta \equiv (a - a_{\text{exp}})/a_{\text{exp}} = 0$.

31. Brous, J., Fankuchen, I. & Banks, E. Rare earth titanates with a perovskite structure. *Acta Crystallogr.* **6**, 67–70 (1953).
32. Wang, H.-H., Fleet, A., Brock, J. D., Dale, D. & Suzuki, Y. Nearly strain-free heteroepitaxial system for fundamental studies of pulsed laser deposition: EuTiO$_3$ on SrTiO$_3$. *J. Appl. Phys.* **96**, 5324–5328 (2004).
33. Kugimiya, K., Fujita, K., Tanaka, K. & Hirao, K. Preparation and magnetic properties of oxygen deficient EuTiO$_{3-\delta}$ thin films. *J. Magn. Magn. Mater.* **310**, 2268–2270 (2007).
34. Chae, S. C. *et al.* Magnetic properties of insulating RTiO$_3$ thin films. *J. Electroceram.* **22**, 216–220 (2009).
35. Fujita, K., Wakasugi, N., Murai, S., Zong, Y. & Tanaka, K. High-quality antiferromagnetic EuTiO$_3$ epitaxial thin films on SrTiO$_3$ prepared by pulsed laser deposition and postannealing. *Appl. Phys. Lett.* **94**, 062512 (2009).
36. Hatabayashi, K. *et al.* Fabrication of EuTiO$_3$ epitaxial thin films by pulsed laser deposition. *Jpn. J. Appl. Phys.* **48**, 100208 (2009).
37. Theis, C. D. & Schlom, D. G. Cheap and stable titanium source for use in oxide molecular beam epitaxy systems. *J. Vac. Sci. Technol. A* **14**, 2677–2679 (1996).
38. Schlom, D. G. *et al.* Strain tuning of ferroelectric thin films. *Annu. Rev. Mater. Res.* **37**, 589–626 (2007).
39. Steins, M., Doerschel, J. & Reiche, P. Crystal structure of aluminium lanthanum strontium tantalum oxide, (La$_{0.272}$Sr$_{0.728}$)(Al$_{0.648}$Ta$_{0.352}$)O$_3$. *Z. Kristallogr. New Cryst. Struct.* **212**, 77 (1997).
40. Hellwege, K.-H. & Hellwege, A. M. (eds) *Landolt-Börnstein: Numerical Data and Functional Relationships in Science and Technology* New Series, Group III, Vol. 16a 59 (Springer, 1981).
41. Koster, G. & Kropman, B. L. Rijnders, G. Blank, D. H. A. & Rogalla, H. Quasi-ideal strontium titanate crystal surfaces through formation of strontium hydroxide. *Appl. Phys. Lett.* **73**, 2920–2922 (1998).
42. Veličkov, B. Kahlenberg, V. Bertram, R. & Bernhagen, M. Crystal chemistry of GdScO$_3$, DyScO$_3$, SmScO$_3$, and NdScO$_3$. *Z. Kristallogr.* **222**, 466–473 (2007).
43. Anisimov, V. I., Aryasetiawan, F. & Lichtenstein, A. I. First-principles calculations of the electronic structure and spectra of strongly correlated systems: the LDA+U method. *J. Phys. Condens. Matter* **9**, 767–808 (1997).
44. Kresse, G. & Hafner, J. *Ab initio* molecular dynamics for liquid metals. *Phys. Rev. B* **47**, 558–561 (1993).
45. Blochl, P. E. Projector augmented-wave method. *Phys. Rev. B* **50**, 17953–17979 (1994).
46. Kresse, G. & Furthmuller, J. Efficient iterative schemes for *ab initio* total-energy calculations using a plane-wave basis set. *Phys. Rev. B* **54**, 11169–11186 (1996).
47. Kresse, G. & Joubert, D. From ultrasoft pseudopotentials to the projector augmented-wave method. *Phys. Rev. B* **59**, 1758–1775 (1999).